

# In Vivo Measurement of Cortical Impedance Spectrum in Monkeys: Implications for Signal Propagation

Nikos K. Logothetis,<sup>1,2,\*</sup> Christoph Kayser,<sup>1</sup> and Axel Oeltermann<sup>1</sup>

<sup>1</sup>Max Planck Institute for Biological Cybernetics, Spemannstrasse 38, 72076 Tübingen, Germany

<sup>2</sup>Division of Imaging Science and Biomedical Engineering, University of Manchester, Manchester M13 9PT, UK

\*Correspondence: [nikos.logothetis@tuebingen.mpg.de](mailto:nikos.logothetis@tuebingen.mpg.de)

DOI 10.1016/j.neuron.2007.07.027

## SUMMARY

To combine insights obtained from electric field potentials (LFPs) and neuronal spiking activity (MUA) we need a better understanding of the relative spatial summation of these indices of neuronal activity. Compared to MUA, the LFP has greater spatial coherence, resulting in lower spatial specificity and lower stimulus selectivity. A differential propagation of low- and high-frequency electric signals supposedly underlies this phenomenon, which could result from cortical tissue specifically attenuating higher frequencies, i.e., from a frequency-dependent impedance spectrum. Here we directly measure the cortical impedance spectrum in vivo in monkey primary visual cortex. Our results show that impedance is independent of frequency, is homogeneous and tangentially isotropic within gray matter, and can be theoretically predicted assuming a pure-resistive conductor. We propose that the spatial summation of LFP and MUA is determined by the size of these signals' generators and the nature of neural events underlying them, rather than by biophysical properties of gray matter.

## INTRODUCTION

Behavior, with all its variety and complexity, reflects the coordinated activity of neurons that are organized into local and global networks. To understand the spatiotemporal organization of activity in such networks and the way it generates behavioral output, we need to combine results derived from its measurements at different spatial scales, including large-scale information provided from neuroimaging methods, regional information derived from mesoscopic electrical activity, such as that obtained from field potentials, and information on the activity of single neurons, traditionally obtained from fine-resolution, extracellular, single-unit recordings.

For several decades, combined electrophysiological and behavioral experiments have concentrated mainly on the finest of these scales, ignoring other graded signals, population synchrony, and rhythms yielding medium to large-scale activation patterns. Ever since their development (Adrian and Zotterman, 1926), in fact, microelectrodes have been used to monitor the spiking rate of isolated neurons, and this rate was used as the neural correlated of behavior (for a review, see Logothetis, 2002; Logothetis and Wandell, 2004). The focus on spiking rates remained unchallenged for many decades and was strengthened by their suitability for studying the first steps of afferent information processing in sensory physiology (Hubel and Wiesel, 1962; Kuffler, 1953; Lettvin et al., 1959). The very same microelectrodes, however, can also be used to monitor the slow (<120 Hz) potential changes that are generated by all regional sinks and sources within the extracellular space. They typically, but not exclusively, provide three-dimensional information about the cooperating synaptic inputs into a recorded area; such information is often not predictable from spiking activity. Such mesoscopic recordings may prove essential for the study of small networks and the interactions between distant brain regions (Abeles, 1991; Bullock, 1997; Freeman, 1975).

The importance of understanding small networks, rather than merely focusing on single cell properties, can hardly be overestimated. Every cortical pyramidal cell receives approximately 10,000 synaptic inputs, about 75% of which are excitatory, the exact numbers varying between structures and species (Abeles, 1991; Braitenberg and Schüz, 1998). The vast majority of these excitatory inputs arise from other cortical neurons, with each presynaptic cell providing only a few synapses. The strong convergence of synaptic input onto each cortical cell shows the degree of integration at the single-cell level and gives us an indication of the complexity of the computations performed at each recording site. These computations ultimately determine the properties of the canonical cortical microcircuits (Douglas et al., 1989; Douglas and Martin, 1990, 1991), the elementary processing units of cortex.

The study of such units and of the computations they perform can greatly benefit from the analysis of the local field potentials (LFPs). Until recently the latter were thought to be generated by summed (population)

postsynaptic potentials, as first proposed by Eccles (1951). Indeed, intracellular recordings from cortical neurons demonstrated a close correspondence between LFP and EEG activity and synaptic potentials (Creutzfeldt et al., 1966; Morocutti et al., 1966; Watanabe et al., 1966). At the same time, such measurements also showed that the slow wave activity in the EEG is largely independent of neuronal spiking responses (Ajmone-Marsan, 1965; Buchwald et al., 1965; Fromm and Bond, 1967). The observation that slow wave potentials but not spiking activity is visible at the scalp surface was interpreted as an indication that cortical tissue possesses strong frequency-filtering properties (Bedard et al., 2004, 2006).

Such frequency-dependent behavior was also suggested by experiments employing the typical extracellular unit recordings. Under most conditions, the amplitude of extracellularly recorded spikes is very sensitive to the position of the electrode (Gold et al., 2006), while slow potentials show much less sensitivity to position. In addition, the spatial correlation of slow waves is found to extend over larger cortical distances (>7 mm) than that of the higher frequencies such as the gamma band (24–90 Hz) or spiking activity (Destexhe et al., 1999). This differential spatial correlation provides additional support for the hypothesis that cortical tissue selectively filters frequencies; in other words, it suggests that cortical tissue has a non-flat impedance spectrum. A frequency-dependent impedance spectrum could selectively attenuate electric signals of some frequencies more than those of others—for example, high-frequency spiking events more than low-frequency potentials (Bedard et al., 2004, 2006; Destexhe et al., 1999).

The simplest way to examine the cortical frequency-filter hypothesis is to measure the impedance spectrum directly. Impedance is a measure of the ability of a circuit to resist the flow of electrical current. In biological tissues the “circuit” is the volume conductor, consisting of various intra- and extracellular components of the brain tissue, and the “current” is generated by the movement of ions. Measurements of biological impedances have proved highly useful in understanding the propagation of electromagnetic waves in the body (Schwan, 1963, 1999), in identifying different brain regions under different physiological conditions, e.g., hypoxia (Van Harrevel and Ochs, 1956), and in determining the anatomical and electrical characteristics of the cells, the interstitial space, and their interrelations (Freygang and Landau, 1955; Havstad, 1976; Ranck, 1963a). In basic and clinical neurosciences, the bioimpedance research provides information about the conductivity of tissues and helps the design of better models for electric currents and conductivity tensors, with very useful applications, including impedance encephalography and impedance tomography. Such models have been often used for the study of electrical injury mechanisms and pathology and can be also used to better understand the propagation of different neural signals.

In the present study, precise measurements of the impedance of cortical tissue within gray and white matter

of the monkey visual cortex showed no frequency dependence, regardless of the direction or depth of measurement. Our measurements were carried out using a novel, custom-made system that permits unbiased computation of cortical impedance using a five-point measurement technique. On the basis of our measurements and of concomitant simulations, we conclude that the cortical tissue has the properties of a simple ohmic conductor, which permits unbiased propagation of signals of any biologically relevant temporal frequency.

## RESULTS

The histological properties of brain tissue by themselves make it clear that the brain is not a homogeneous and isotropic medium. Most obvious, of course, are the differences in the histological properties of the gray and white matter, and it comes as not surprise that they also differ in electric resistance. Within a particular cortical area, however, the gray matter seems rather homogenous in a tangential direction, while cell density and myelination differ across layers, i.e., in a radial direction. Here we directly measured the cortical impedance spectrum in gray and white matter as well as along different tangential directions and in a radial direction.

### The Impedance Spectrum in the Tangential Plane

Figure 1 shows the frequency response of the cortical tissue in a series of measurements along tangential directions. The interelectrode distance was 3 mm, and the tip of the electrodes was 250  $\mu\text{m}$  deep in the cortex (Figure 1A). Figure 1B displays the results for monkey B02. The initial impedance of the electrodes at 1 kHz was 450 k $\Omega$  and 70 k $\Omega$  for the two current electrodes, and 130 k $\Omega$  and 140 k $\Omega$  for the voltage electrodes, respectively. We tested frequencies in the range of 10 Hz to 5 kHz and different stimulation currents (see color code). As the figure clearly shows, the amplitude of the cortical resistance drops by only 1.9 dB as the frequency increases from 10 Hz to 5 kHz. For comparison purposes the figure also displays the frequency responses of a 20  $\mu\text{F}$  and a 1.26  $\mu\text{F}$  capacitor (dotted lines). The impedance of a capacitor drops by 6 dB when the frequency is only doubled. In the range of 10 Hz to 5 kHz, the drop for the 20  $\mu\text{F}$  capacitor is 49.4 dB, which is much larger than the drop observed for the cortical tissue.

The deviation from a completely flat response might be the result of measuring errors, or alternatively, a very small (practically insignificant) dependence on frequency may be a property of the tissue. In saline a drop of 1 dB from lower to higher frequencies is also typical (see below).

The reproducibility of the measurements was verified by repeated measurements at the same cortical depth (250  $\mu\text{m}$ ) and using the same current (the three thick lines in Figure 1B, Reps1–3). The three repeats differ from each other by a maximum of 0.2 dB, demonstrating the high reliability of the measurement. In addition, we tested the linearity of the tissue by repeatedly lowering the current by

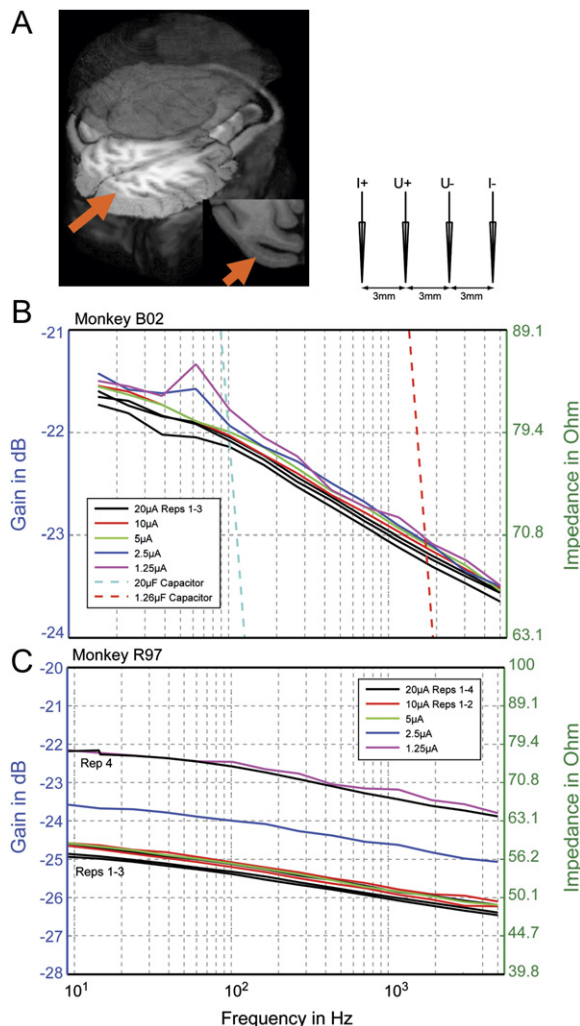


**Figure 1. Signal Attenuation as a Function of Frequency**

The figure shows the cortical impedance spectrum of two monkeys (B02, R97).

(A) Typical location in cortex (primary visual cortex) at which impedance was measured. The electrodes were spaced at equidistant intervals (3 mm) and with all tips at the same depth (250  $\mu$ m deep from the dura).

(B and C) The impedance for each animal and different stimulation currents (see insets). The frequency range tested was 10 Hz to 5 kHz (abscissa), and the left ordinate denotes the signal gain in decibels, defined as  $20 \cdot \log(U_{\text{rec}}/U_{\text{drive}})$ , where  $U_{\text{drive}}$  is the "target" signal driving the voltage-to-current converters, and  $U_{\text{rec}}$  is the recorded voltage drop across the tissue. The higher the tissue impedance, the higher the expected signal gain. The right ordinate shows the computed impedance values for each of the gain levels. It is evident from all traces that gain is independent of frequency, with a maximum drop of 1.9 dB for a frequency increase from 10 Hz to 5 kHz. For comparison, the frequency responses of a 20  $\mu$ F and a 1.26  $\mu$ F capacitors are also plotted as dotted lines. Note that the value of capacitance influences only the position of the gain-to-frequency function with respect to the abscissa of the plot because of the well-known relationship  $R_c = 1/(2\pi \cdot f \cdot C)$ . The slope of the line in the log-log plot remains the same. That is, should the cortical tissue have capacitive properties, one would expect the curves derived from different current applications to have

factors of two from 20  $\mu$ A down to 1.25  $\mu$ A. No noticeable nonlinearities of the extracellular tissue were evident throughout the tested current range. The small signal increase in the two curves with the lowest current, around 60 Hz, is probably due to interference from the 50 Hz power supply; this interference is stronger because of the reduced signal-to-noise ratio at the low currents.

Figure 1C shows the results of the same experiment with the second animal (R97). At the beginning of the experiment, three spectra were measured consecutively with an excitation current of 20  $\mu$ A peak value. As shown in Figure 1C, the responses are flat within 1.5 dB, and the maximum difference between repeats is 0.33 dB. Testing linearity with different currents revealed the same results as with the animal B02, and most currents yielded very similar impedance spectra. Surprisingly, the responses obtained with the 2.5  $\mu$ A and 1.25  $\mu$ A currents were 1 dB and 2 dB higher than the response at 5  $\mu$ A, an observation that would seem to suggest the existence of a nonlinearity (current-dependant resistance). However, repeating a measurement with a 20  $\mu$ A current immediately after the measurement with 1.25  $\mu$ A revealed that the 1.25  $\mu$ A and 20  $\mu$ A spectra overlapped. This strongly suggests that the difference probably results from a slight movement of the electrode or cortical tissue in, between, or during the 2.5 and 1.25  $\mu$ A measurements, but not from a current dependency of the impedance spectrum.

The notion that the gray matter impedance spectrum is flat for all directions is further corroborated by measurements at different distances from the surface (point of penetration in the dura mater) and different orientations of the electrodes. In Figure 2, all four electrodes were advanced in seven steps from 250  $\mu$ m to 3250  $\mu$ m, and the impedance spectrum was recorded using an excitation current of 20  $\mu$ A peak. Within the gray matter (approximately depths above 2000  $\mu$ m), the spectrum is clearly flat for all depths, and the drop-off is less than 2.0 dB within the range of 10 Hz to 5 kHz. Importantly, the same flat impedance behavior was found for measurements where the four-electrode system was oriented in a mediolateral direction (Figure 2B) and in an anterior-posterior direction (Figure 2C) in the same animal. This not only demonstrates a flat impedance spectrum, but also reveals comparable impedance in different tangential directions, suggesting that the impedance spectrum is isotropic within the tangential plane.

the same slope as the dotted green and red lines shown in the plot. For both animals, the reproducibility of the measurements was verified by repeated-measurements at the same cortical depth (approximately 250  $\mu$ m). For monkey R97 four spectra were acquired with the same excitation current of 20  $\mu$ A, three at the beginning and one at the end of the experimental session. The first three sequential repetitions yielded entirely overlapping traces. In the fourth repetition (and for the lower currents), although the spectral power distribution remained the same, the overall impedance changed slightly, probably due to small asymmetric movements of the tissue with respect to the electrode tips (e.g., retraction of the dimpled dura).

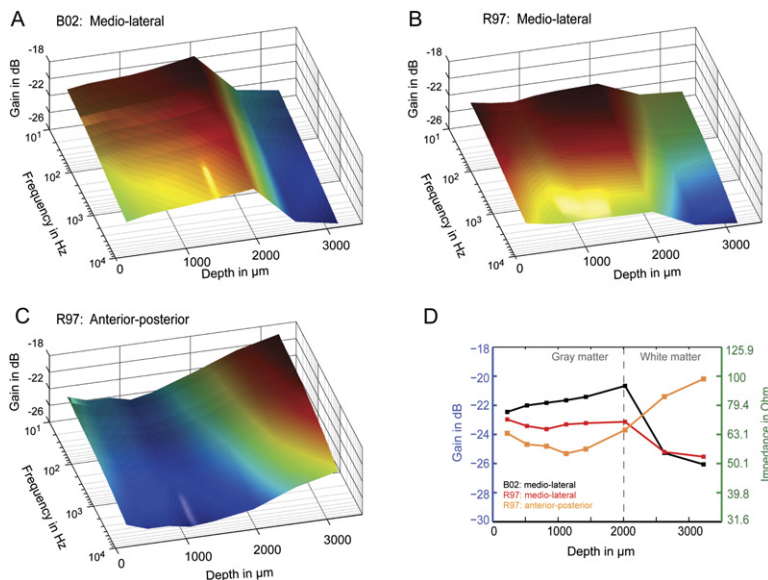


**Figure 2. Impedance Spectra at Different Depths from the Pial Surface**

The interelectrode distance was 3 mm, as in Figure 4, and nine spectra were acquired in the range of 250–3250  $\mu\text{m}$ .

(A and B) Data from the two animals, with the electrode array approximately parallel to the mediolateral direction. Both plots show no significant change of impedance with frequency in any of the depths at which measurements were conducted.

(C) Repetition of the experiment in monkey R97 with the electrode array approximately along the anterior-posterior axis. The results are similar. In all three surface plots, an abrupt change occurs only at the transition between gray and white matter, but the frequency response even in white matter remains largely flat.

(D) Shows the average impedance (over all frequencies) as a function of cortical depth. Note that the impedance of white matter may be greater or smaller than that of the gray matter, depending on the orientation of the electrode array.

However, when advancing the electrodes into white matter—a transition that was also verified electrophysiologically—we consistently noticed an abrupt change in impedance. Importantly, the impedance of the white matter showed a strong dependency on the direction of measurement: while measurements in the mediolateral direction revealed a decrease of impedance at the gray-white matter transition (Figure 2B), measurements in the anterior-posterior direction revealed an increase (Figure 2C). Importantly, the impedance spectrum of the white matter was again frequency independent, and all measured values were within 2.5 dB in the measured frequency range. This anisotropy of the white matter, as well as the isotropy of the gray matter, are also clearly evident in Figure 2D, which displays the average impedance (over all frequencies) as a function of cortical depth.

In addition to testing the frequency responses of the cortical tissue, we also examined the phase shift between the voltage and the excitation current at four different cortical depths. Figure 3 shows nearly zero phase shift at low frequencies and a drop to about  $-13^\circ$  at higher frequencies. As these numbers are not intuitively clear, we compared them to the phase shift observed in a resistive load (simple resistor) and in saline. The resistor showed a drop of  $-5.5^\circ$ , while measurements in saline typically yielded a drop of about  $-10^\circ$ . Given the similarity of the numbers obtained in gray matter and saline, we conclude that there is no significant phase shift in cortex between the current and the voltage, independent of frequency and depth.

### The Impedance Spectrum in the Radial Direction

Impedance measurements were also conducted between points at different cortical depths, hence in a radial direction. For such measurements the interelectrode distance

must be optimized to permit the crosstalk-free measurement of points differing as little as possible along the horizontal direction. Measurements from sulci were impractical with respect to precise placement of the electrode arrays. Instead, a special electrode arrangement and a modified electrode drive were used for measurements in the gyral cortex. A commercial seven-electrode drive (Thomas Recording, GmbH, Giessen) was modified, both mechanically and electronically, to ensure compatibility with the previous measurements. In addition, to avoid crosstalk between the electrode wires, metal plates were added between every electrode wire inside the shielded drive case.

Figure 4 illustrates the impedance spectra recorded at different depths and radial electrode distances. For each

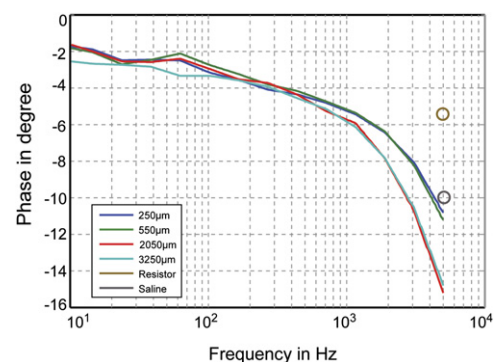


**Figure 3. Effects of Frequency on Signal Phase**

The figure shows the phase shift as a function of frequency. The interelectrode distance is 3 mm, and depth ranges from 250 to 3250  $\mu\text{m}$ . All curves show a modest phase shift that is comparable with the shift observed in control experiments conducted in a saline bath and with an ohmic resistor (circles).



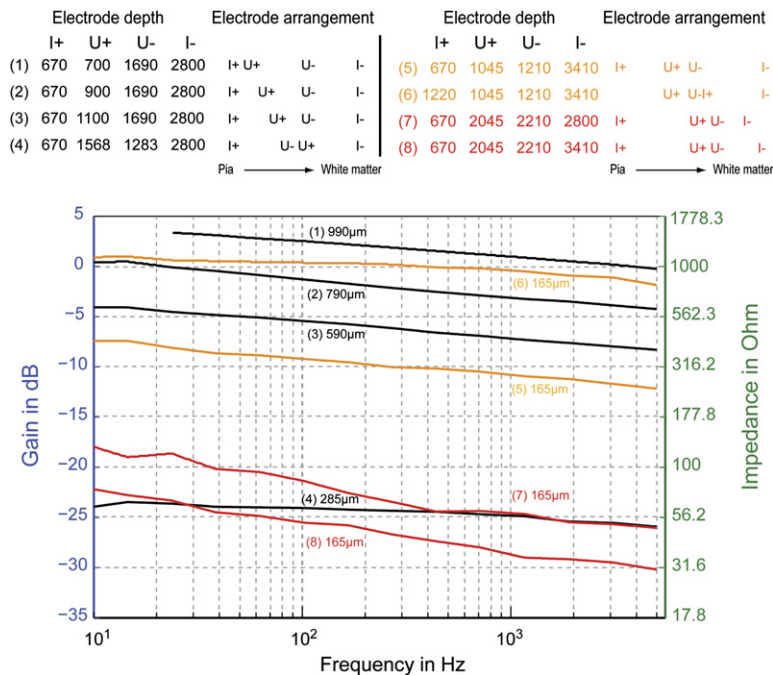


**Figure 4. Impedance at Different Cortical Depths**

Measurements of impedance between points at different depths with respect to the dura (radial direction). For each measurement (defined by the numbers), the quadruples indicate the depths of the I+, U+, U-, and I- electrode tips and their relative positioning. During measurements 1–3 (black) the distance between the voltage electrodes was lowered, and in measurement 4 the order of U+ and U- was changed. In these measurements the distance of the current electrodes was fixed at 2130  $\mu\text{m}$ . Predictably, impedance decreases with decreasing distance between the voltage electrodes. For measurements 5–8 (orange and red) the distance of the voltage electrodes is fixed (165  $\mu\text{m}$ ), but in 5 the voltage electrodes are in between the current electrodes, while in 6 they are not. Between 7 and 8 one current electrode was moved closer to the voltage electrodes.

measurement, the upper panel indicates the depths of the electrode tips and shows a sketch of their relative alignment. In the first series (black lines, 1–4) the current electrodes had a fixed distance of 2130  $\mu\text{m}$ , while the distance between the voltage electrodes was varied by lowering the U+ electrode (measurements 1–3) and by reversing the position of the voltage electrodes (4). Again, the frequency dependence of the impedance spectra was small, regardless of the distance between the electrodes. This demonstrates that the conductivity of the gray matter is frequency independent along the radial direction.

In addition, these measurements confirm that the approximation of the cortical tissue by a series of impedances, as depicted in Figure 7C (Experimental Procedures), is only an approximation. For example, changing the distance between the voltage and current electrodes while keeping the distance of the two voltage electrodes fixed (orange lines 5–6 and red lines 7–8) alters the measured signal gain. From 5 to 6 the arrangement of the electrodes was altered altogether, and the voltage electrodes were no longer positioned in between the current electrodes. From 7 to 8 one current electrode was moved further away from the voltage electrodes. In both cases, the measured signal gain is larger when the current electrode is closer to the voltage electrodes which would not be expected from the simple three-resistor model. This results from a larger electric potential induced at the voltage electrode when the stimulating electrodes are closer (see theoretical analysis in the following section), and hence shows that the distance between the current and the voltage electrode cannot be approximated easily by simple impedances ( $Z_+$ ,  $Z_T$ , and  $Z_-$ ), as shown in Figure 7D. More importantly, these measurements confirm that the

flat impedance spectrum does not result from a specific arrangement of the measurement system, and they support the theoretical arguments provided below.

Our results have certain implications with respect to signal propagation in cortex and the relative spatial specificity of action and field potentials. To obtain a better understanding of these, the following section provides a theoretical analysis of the currents and potentials for sources in a homogenous and isotropic ohmic medium and for similar electrode configurations as used in the in vivo and in vitro experiments.

### Theoretical Analysis of Signal Propagation in the Extracellular Space

Neurons are considered to be embedded in an extracellular medium that acts as a volume conductor (Lorente de Nó, 1947) (for a detailed review on field potentials, see Freeman, 1975); for background in biophysics, see Aidley, 1989; Johnston and Wu, 1995). When the membrane potential between two separate regions of such a neuron differs, there is a flow of current in the neuron matched by a return current through the extracellular path. Active regions of the membrane are considered to act as a current *sink*, inactive ones as a *source* for the active regions. Such extracellular field potentials add up linearly and algebraically throughout the volume conductor (the principle of electric superposition).

Inside the physiological frequency range (0 to about 5 kHz), the inductive, magnetic, and propagative (wave) effects of the bioelectrical signals in the extracellular space can be neglected (Aidley, 1989; Robinson, 1968), permitting the description of the current electrode as a simple static point source (McIntyre and Grill, 2001) that can be

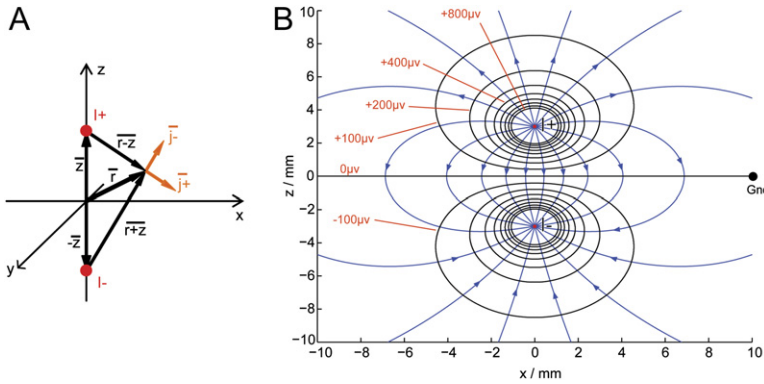


**Figure 5. Field Induced by Bipolar Stimulation**

(A) Illustrates the coordinate system we used for simulations (see text).

(B) Equipotential surfaces (black curves) and streamlines of the current (blue curves)—representing a slice of the three-dimensional current flow field—for an electric dipole. The plot illustrates the numerical solution of the equations Equation 3 and 4 with dimensions taken from a real experiment described in the text.

described using Ohm's law. As detailed in the [Supplemental Data](#) available with this article online, using Ampere's law one can derive the following expressions for the electric potential  $U$  and the current density  $j$  of a point source (which is assumed to be at the origin of the coordinate system):

$$\vec{j}(\vec{r}) = \frac{I}{4\pi} \cdot r^{-2} \cdot \vec{e}_r \quad (1)$$

$$U(r) = \frac{1}{4\pi} \frac{I\rho}{r} \quad (2)$$

whereby  $\vec{e}_r$  is the unity vector in the radial direction,  $\vec{r}$  denotes the position vector,  $I$  is the current, and  $\rho$  is the specific electric resistance (also known as electrical resistivity).

To obtain the electric potential in the field induced by two current sources, one acting as source (I+) and one as sink (I-) as in our in vivo experiments, we can use the principle of superposition. Using the coordinate system depicted in [Figure 5](#), and taking the distance between the electrodes as  $2z$  [with  $\vec{z} = (0, 0, z)$ ]:

$$\vec{j}(\vec{r}) = \vec{j}_+(\vec{r}) + \vec{j}_-(\vec{r})$$

with

$$\vec{j}_+(\vec{r}) = \frac{I}{4\pi} \cdot |\vec{r} - \vec{z}|^{-2} \cdot \frac{\vec{r} - \vec{z}}{|\vec{r} - \vec{z}|}$$

and

$$\vec{j}_-(\vec{r}) = \frac{-I}{4\pi} \cdot |\vec{r} + \vec{z}|^{-2} \cdot \frac{\vec{r} + \vec{z}}{|\vec{r} + \vec{z}|},$$

whereby the fractions represent the current directions  $\vec{e}_r$ . Combining these equations, we obtain

$$\vec{j}(\vec{r}) = \frac{I}{4\pi} \left[ \frac{\vec{r} - \vec{z}}{|\vec{r} - \vec{z}|^3} - \frac{\vec{r} + \vec{z}}{|\vec{r} + \vec{z}|^3} \right] \quad (3)$$

Similarly, we add the voltage from single electrodes (Equation 2) to obtain the total voltage of the dipole:

$$U(\vec{r}) = U_+(\vec{r}) + U_-(\vec{r}) = \frac{1}{4\pi} I \rho \left[ \frac{1}{|\vec{r} - \vec{z}|} - \frac{1}{|\vec{r} + \vec{z}|} \right] \quad (4)$$

The graphical representation of the results of Equations 3 and 4 are shown in [Figure 5B](#), with the constants taken from saline-bath experiments [see section 4.4:  $\rho = 0.664 \, \Omega \text{m}$ ,  $z = 3 \text{ mm}$ ,  $I = 20 \, \mu\text{A}_{\text{pk}}$ , the I+ electrode at  $(0, +3 \text{ mm})$  and the I- electrode at  $(0, -3 \text{ mm})$ ]. To illustrate the dipole field, [Figure 5B](#) shows 17 isopotential lines from  $-800 \, \mu\text{V}$  to  $+800 \, \mu\text{V}$  in the x-z plane, as well as the streamlines of the current vector field.

This electrode configuration can be used to simulate the signal propagation in the brain. The I+ and the I- electrodes form a floating current source similar to a neuron. The current flows through the intracellular tissue in a manner similar to that illustrated in [Figure 5](#). Perpendicular to this current direction there is a voltage potential that can be graphically depicted by the equipotential lines (circular lines in [Figure 5B](#)). Because the current source is floating and the point sources symmetrical, the center voltage line has zero volts, just like a distant, remote ground (Gnd). The sign of the recorded signal depends on the location of the recording electrode with respect to the zero-volt line. When the voltage is measured across two conductors (U+, U-), one at each side of the zero line, the amplitude of the voltage, as expected, will be twice as large. All above-mentioned relationships were examined by using our system and conducting measurements in saline.

### Experiments in Saline and In Vitro

We performed systematic experiments in a saline bath using the same measurement system as used in the in vivo experiments. [Figure 6A](#) shows the electrode configuration used in the saline experiments. There were two current electrodes, I+ and I-, and two voltage-sensing electrodes,  $U_a$  and  $U_b$ , in the x-z plane. From [Figure 6A](#) we derive that  $\vec{z} = (0, 0, z)$ ;  $\vec{r}_a = (d, 0, z)$ ;  $\vec{r}_b = (d, 0, -z)$ , where  $d$  is the distance between voltage and current electrodes. Let  $U_{a+}$  denote the voltage at electrode  $U_a$  induced by the current electrode I+ and  $U_{a-}$  denote the voltage at the same point induced by electrode I- (similar for  $U_b$ ).

By inserting the vectors in Equation 2, we obtain

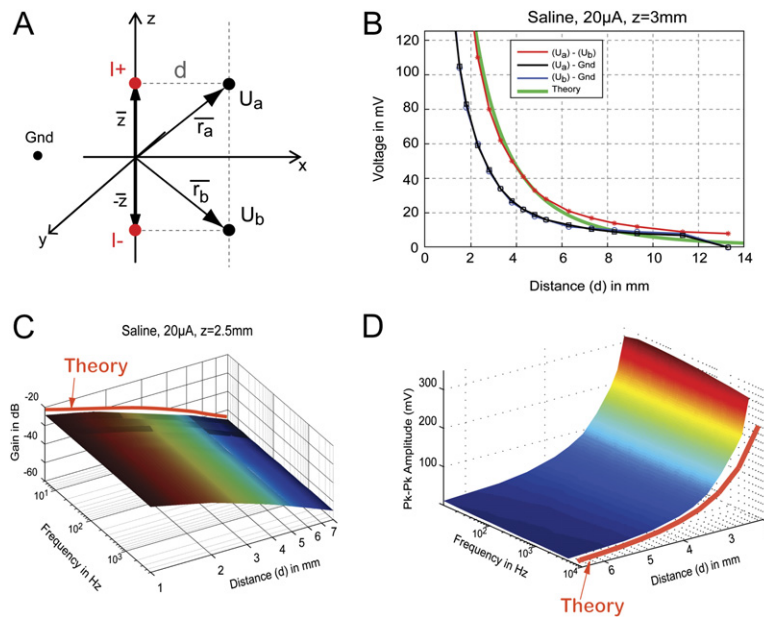


**Figure 6. Volume Conduction in Saline and in the Brain Tissue**

The figure shows the impedance spectrum for measurements in saline.

(A) Coordinate system for measurements in a saline bath. The voltage electrodes were aligned parallel to, but offset from, the current electrodes (with a distance parameter  $d$ ).

(B) Measured voltage across the voltage electrodes ( $U_a$  to  $U_b$ , red), voltage of  $U_a$  and  $U_b$  with respect to ground (blue and black), as well as the theoretical result for the voltage between  $U_a$  and  $U_b$  (green). The data show that the saline bath behaves as predicted from the theoretical arguments.

(C) Impedance spectrum of the saline bath as a function of stimulation frequency and electrode distance (parameter  $d$ ). The spectrum is flat, and the impedance changes only with electrode distance but not with frequency.

(D) Shows measurement in pig cortex. For details see text.

$$U_{a+}(\vec{r}_a) = \frac{1}{4\pi} I \rho \frac{1}{d}; \quad U_{a-}(\vec{r}_a) = -\frac{1}{4\pi} I \rho \frac{1}{\sqrt{d^2 + 4z^2}}$$

and

$$U_{b+}(\vec{r}_b) = \frac{1}{4\pi} I \rho \frac{1}{\sqrt{d^2 + 4z^2}}; \quad U_{b-}(\vec{r}_b) = -\frac{1}{4\pi} I \rho \frac{1}{d}$$

from which we can compute the differential voltage as

$$U = (U_{a+} + U_{a-}) - (U_{b+} + U_{b-}) = \frac{I\rho}{2\pi} \cdot \left( \frac{1}{d} - \frac{1}{\sqrt{d^2 + 4z^2}} \right) \quad (5)$$

Figure 6B shows the result of such a measurement in saline. The distance ( $2 \cdot z$ ) between the two current electrodes and that between the two voltage electrodes was always equal to 6 mm. The distance between the current and the voltage electrodes ( $d$ ) was variable, with a minimum distance of 1.5 mm. The excitation current was 20  $\mu$ A peak value and 100 Hz sinusoidal. The red curve is the peak-to-peak (pk-pk) voltage across the  $U_a$  and the  $U_b$  electrodes measured after preamplification (gain of 100). The blue and the black curves (almost superimposed) show the voltages of the  $U_a$  and  $U_b$  electrodes, respectively, referenced to the remote ground. The opposite sign of the voltages  $U_a$  and  $U_b$  cannot be discerned because the inputs are sinusoidal. The difference between the voltage electrodes (red trace) is twice as large as the single voltages, as expected.

The green line displays the result expected from the theoretical considerations above (Equation 5) and closely matches the measured values of the differential voltages. The parameters were obtained from the actual experiments ( $z = 3$  mm,  $I = 20$   $\mu$ A<sub>0-pk</sub>,  $\rho = 0.664$   $\Omega$ ). In addition, the value of  $\rho$  was measured with precision using another more accurate method (not described here). The result of

Equation 5 was doubled to reflect the peak-to-peak measurements and was multiplied by 100 to account for the amplification factor.

Using the configuration we have just described, we examined the frequency dependence of signal propagation for different interelectrode distances (Figure 6C). The frequency spectrum was recorded in a frequency range from 10 Hz to 5 kHz and using a sinusoidal excitation current of 20  $\mu$ A. For all nine different distances ( $d$ ) from the current to the voltage electrodes the frequency response is flat, i.e., independent of frequency. For each distance the measured values were within 2 dB across frequencies. In addition, the gain changes with the distance ( $d$ ) between the voltage and current electrodes as the potential difference (Equation 5) changes with this parameter; the same behavior was seen in the *in vivo* experiments (see Figure 6D).

At last, the measurements taken in saline were repeated in brain tissue. We have measured the voltage drop as a function of distance in fresh pig brains (commercially available a few hours after slaughter). Pig rather than monkey brains were used to achieve maximum mechanical precision in electrode positioning and avoid unnecessary repeated penetrations in regular experimental primates contributing to other projects. The brains were placed in a custom-made, form-specific container, and the dura was removed. Measurements were conducted in regions void of sulci and large vessels. We used the same parameters with those employed in the saline measurements in Figure 6B, barring the distance between the electrodes, which was  $2 \cdot z = 2$  mm (see Figure 6A). Equation 5 was used to describe the theoretically expected voltage-to-distance relationship ("Theory" curve in Figure 6D). For the calculation of this curve we used a resistivity value of  $\rho = 2.56$   $\Omega$ m that best matched theory with experimental

data. This value was approximately in the middle of the range of resistivities, (1.65  $\Omega\text{m}$  3.29  $\Omega\text{m}$ ), for all measured depths [200  $\mu\text{m}$  1700  $\mu\text{m}$ ] in the gray matter of monkeys. As can be seen in Figure 6D, the impedance spectrum is flat and independent of the distance of the voltage to current electrodes. In addition, for each of the frequencies tested the voltage across the voltage electrodes drops as predicted by the theoretical analysis, and the absolute voltage values correspond to those obtained by theory when resistivity is set equal to that measured in monkeys.

### Computing the Specific Resistance

To compute the specific resistance for brain tissue and saline, we apply our theoretical considerations to exactly the same electrode configuration as used in the in vivo experiments. The current and the voltage electrodes are placed in one row with constant distance  $a$  (Figure S1). From the picture one derives  $z = \frac{3}{2}a$ ;  $\vec{r}_+ = (0, 0, \frac{1}{2}a)$ ;  $\vec{r}_- = (0, 0, -\frac{1}{2}a)$ ;  $\vec{z} = (0, 0, z)$ . Voltages were measured differentially between the  $U_+$  and the  $U_-$  electrode. From Equation 5 the expected voltage is

$$U = U_+(\vec{r}_+) - U_-(\vec{r}_-);$$

$$U_+(\vec{r}_+) = U_+ \left( 0, 0, \frac{1}{2}a \right) \\ = \frac{I\rho}{4\pi} \left[ |\vec{r}_+ - \vec{z}|^{-1} - |\vec{r}_+ + \vec{z}|^{-1} \right] = \frac{1}{8\pi} \frac{I\rho}{a};$$

$$U_-(\vec{r}_-) = U_- \left( 0, 0, -\frac{1}{2}a \right) \\ = \frac{I\rho}{4\pi} \left[ |\vec{r}_- - \vec{z}|^{-1} - |\vec{r}_- + \vec{z}|^{-1} \right] = -\frac{1}{8\pi} \frac{I\rho}{a}$$

$$U = \frac{1}{4\pi} \frac{I\rho}{a}$$

We measured the fraction  $U/I$ , representing the resistance  $R$ , given by  $R = \frac{1}{4\pi} \frac{\rho}{a}$  or simply:

$$\rho = 4\pi a R \quad (6)$$

This equation was used to determine the specific electric resistance  $\rho$  at an electrode distance of  $a = 3$  mm. For saline, the resistance measured was 14  $\Omega$ , yielding a specific resistance of  $\rho = 0.528$   $\Omega\text{m}$ . This is in agreement with the value measured with the precise method mentioned above ( $\rho = 0.664$   $\Omega\text{m}$ ); the small deviation is most likely due to mechanical imprecision during the placement of electrodes. For cortical tissue, we obtained an absolute resistance of 43.8 to 104  $\Omega$  (see Figures 1 and 2), depending on the different measurement parameters. This translates to a specific resistance in a range of  $\rho = 1.65$  to 3.9  $\Omega\text{m}$ .

### DISCUSSION

The methodological developments and experiments described in this paper were motivated by the need for a clear

and definite answer to the following questions: (1) is the cortical tissue of the primate resistive or capacitive in nature, and (2) is its conductivity isotropic? Answering these questions helps us to model and better understand the propagation and spatial summation of extracellular field potentials and hence to bridge the gap between well-localized recordings of single units and recordings of population activity. Our measurements clearly demonstrate that the gray matter is ohmic in nature and has a conductivity that is comparable across directions; the white matter, in contrast, is also ohmic, but its conductivity depends on the direction of measurement.

### The Spread of Population Activity

We have shown that the impedance spectrum of cortex is flat. These results are relevant and important to systems neurophysiology, as they place some constraints on the interpretation of mesoscopic signals such as field potentials. LFPs have been investigated in the context of sensory information processing, with regard to behavioral relevance and motor control, as well as in the context of investigating the origin of the hemodynamic responses (Frien et al., 2000; Gray et al., 1989; Kayser and Konig, 2004; Liu and Newsome, 2006; Logothetis et al., 2001; Mehring et al., 2003; Niessing et al., 2005; Rickert et al., 2005; Scherberger et al., 2005; Wilke et al., 2006; Woelbern et al., 2002). In particular, the amplitude of particular frequency bands of the LFP has been shown to correlate with stimulus features such as a grating's orientation, or with the direction of planned movements. Often such "tuning" is found only in restricted frequency ranges, indicating that LFP frequencies differ in their properties with regard to representing neuronal activity. Similarly, the LFP can be divided into bands that differ in their information content about the stimulus (A. Belitski, A. Gretton, C. Magri, Y. Murayama, M.A. Montemurro, N.K.L., and S. Panzeri, unpublished data), or bands that differ in their power to predict neuronal spiking activity (M. Rasch, A. Gretton, Y. Murayama, W. Maass, and N.K.L., unpublished data). Obviously, the origin and interpretation of these signals are of great importance for understanding the activity and processing within cortical networks.

LFPs were initially thought to reflect population postsynaptic potentials exclusively. Yet, in addition to excitatory and inhibitory postsynaptic potentials (IPSPs and EPSPs), there are a number of possible causes of voltage fluctuations in the brain. For example, one nonsynaptic contributor to the local field is the spike afterpotential, which contributes especially when it is slow and long-lasting like the calcium-mediated potassium current (Nadasdy et al., 1998). Likewise, it is now believed that intrinsic neuronal currents across the cell membrane can show oscillatory behavior and cause changes in the recorded local field potential (Buzsaki, 2002; Chrobak et al., 2000). Similarly, it has been found that, when synaptic activity is blocked, large neuronal populations can show emergent activity that is associated with large (mV) fluctuations in extracellular potentials. While the precise



source of these fluctuations isn't fully understood, it is clear that this nonsynaptic activity can greatly affect the recorded field potential (Buzsaki, 2002; Chrobak et al., 2000).

Despite the ease with which they can be recorded, LFPs have been systematically ignored in most systems neuroscience studies. In part, this is due to the difficulty in interpreting these signals. Optimal mathematical analysis of field potentials requires a knowledge of both the generated fields and the geometry of the neural elements (Nunez, 1981, 1994). Although theoretical calculations are useful, understanding the content of the comprehensive signal acquired by the electrode requires systematic experimentation and a good knowledge of microanatomical cortical architecture. LFPs are usually modeled as arising from a set of current sinks and sources embedded in a homogeneous extracellular medium (Destexhe, 1998; Koch and Segev, 1998; Rall and Shepherd, 1968). This formalism can successfully model several properties of LFPs, but it does not completely account for their apparent frequency-dependent attenuation with distance and hence falls short of explaining their relation to the underlying neuronal events generating these potentials.

### Measuring Tissue Impedance

The extracellular microenvironment consists of narrow gaps between cellular processes, probably not more than 200 Å wide on average. These spaces form a complex three-dimensional mosaic filled with extracellular fluid, and they account for about 12%–25% of the brain's volume (Braitenberg and Schüz, 1998; Peters et al., 1991). Currents and ions spread in this space and, as theoretical reasoning suggests, spread mostly in the extracellular fluid between the cells, but not through them (Robinson, 1968). Hence, the resistance depends on the spatial layout of neurons and glia, resulting in an intricately shaped conductive medium that, in principle, can carry electrical signals over large distances. Confirmation comes from direct measurements of current flow and studies of the diffusion of ions in this microenvironment (Havstad, 1976; Nicholson, 1965; Ranck, 1963a; Van Harreveld et al., 1963; Van Harreveld and Ochs, 1956). However, given the intricate properties of the extracellular medium, it is unclear whether cortical tissue behaves like an ohmic resistor, or whether signals of different frequencies experience frequency-dependent attenuation.

To measure the impedance of cortical tissue directly, one could in principle rely on a two-point measurement system, i.e., use the same electrodes to inject current and measure the voltage drop at the same time. This simple technique is satisfactory as long as the voltage between electrodes is a good approximation of the voltage across the sample. Yet, for tissues of low impedance—on the order of a few hundred ohms—electrode polarization weakens the above approximation (see also below), and for very low frequencies it renders the approximation impossible (Schwan, 1966, 1968). The origin of the problem is in the electrochemistry of the electrode-electrolyte

interface. Briefly, this interface develops into two charged planes of opposite polarity, which in the literal sense forms a capacitor (Geddes, 1997). Since this distance is molecular in dimension, the capacitance is significant. This miniature electrolytic capacitor does not behave like a simple lumped capacitor with constant value. Warburg (1899), who was the first to model the electrode-electrolyte interface as a serially connected resistance  $R$  and capacitance  $C$  (Figure 7D), demonstrated that both  $R$  and  $C$  vary inversely as the square root of the frequency of the current used for measurements (Geddes et al., 1971; Geddes, 1997). Accordingly, measurements of tissue impedance require us to factor out the electrode impedances. The only way of adequately doing this is to use separate electrodes to apply currents and to sample voltages.

In addition, accurate placing of the electrodes with respect to cortical landmarks such as gray-/white-matter boundaries or granulated layers requires the recording of neuronal activity at the same time. Recording of neural activity, however, requires small tip exposures, that is, electrodes with high impedance; commonly impedances of more than 100 k $\Omega$  (at 1 kHz) are necessary to sample multiunit and slow-wave activity. This is in conflict with the prerequisite to use electrodes with impedances that are negligible with respect to the impedance of the tissue, as otherwise the voltage drop across the electrode tips will be whole orders of magnitude larger than the small voltage drop that must be measured across the tissue. Finally, large electrode impedances have large variability. Assuming a coefficient of variation of 10%, an electrode of 100 k $\Omega$ , as measured at 1 kHz, will have variability as high as 10 k $\Omega$ , that is, 2 orders of magnitude higher than the impedance of the tissue.

All in all, the aforementioned caveats preclude the use of a single pair of electrodes for the measurement of tissue impedance. A four-point measurement system can be used instead (Schwan and Ferris, 1968). In such a system two dedicated electrodes are placed with a certain spatial separation and inject a current into the tissue. This current induces a voltage drop depending on the impedance of the tissue, and the drop can be measured using two additional measurement electrodes. This method removes the influence of the electrodes' own impedance on the measurement and allows the use of various geometrical configurations for conducting the measurement within the three-dimensional field created by the current electrodes (c.f. Figure 7).

At last, the electrode-electrolyte interface brings about a second phenomenon that in the present study was used to our advantage. When tungsten electrodes were used, we observed a continuously rising voltage that quickly prohibited proper functioning of our current generator. The behavior of Pt-Ir electrodes was different most likely due to different chemical processes at the metal liquid transition. With Pt-Ir electrodes, during the application of the stimulation current, we observed a voltage-clipping effect: after an initial and rapid increase, the voltage on the current electrodes stabilized (see also Geddes, 1997).

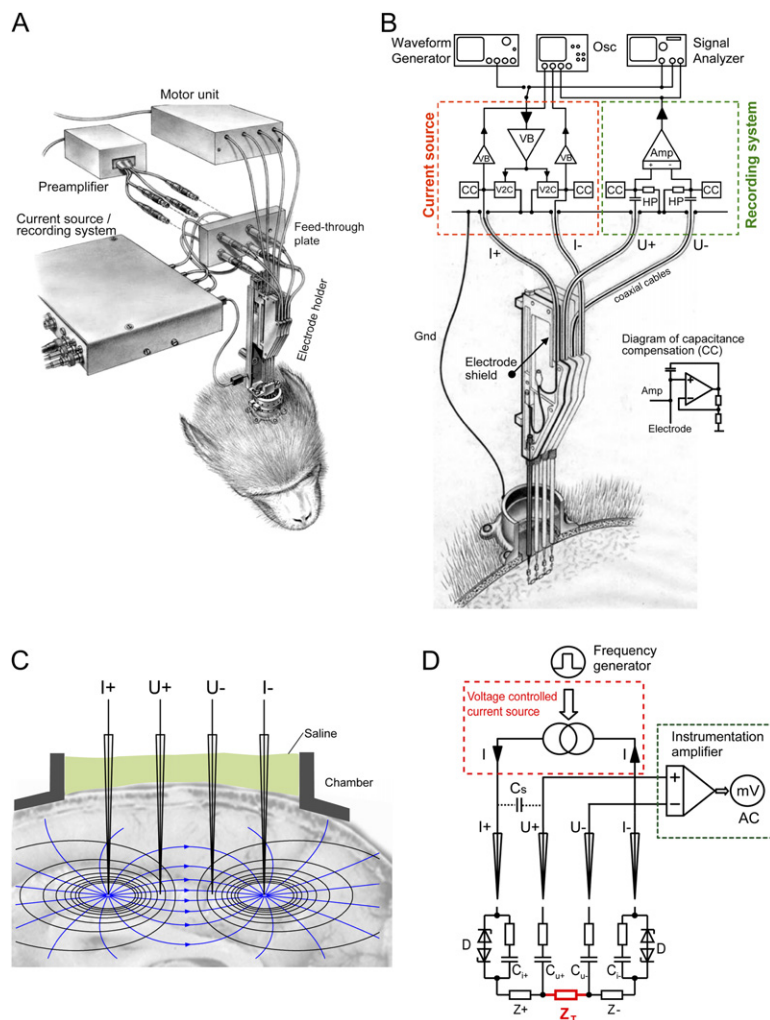


**Figure 7. The Measurement System**

The figure shows the setup used to measure cortical impedance and the corresponding electronic models.

(A) Illustrates the layout of all components, including the electrode holder, the motor units, and the electronic devices.

(B) Shows the arrangement of electrodes within an electrode drive and within the recording chamber and the block diagram of the custom-made electronic circuits, one serving as current source and one serving as recording system. Impedance was measured using separate current (outer electrodes I+ and I-) and voltage (inner electrodes U+ and U-) electrode pairs. The inset in (B) shows the circuit used for the capacitance compensation. CC, capacitance compensation; VB, voltage buffer; HP, high-pass filter; Gnd, ground connection; V2C, voltage to current converter; Amp, instrumentation amplifier; Osc, oscilloscope.

(C) The current source, driven by a frequency generator, creates a three-dimensional current flow (blue lines) between the two current electrodes (I+ and I-). This current reflects a three-dimensional electric potential (black lines) that leads to a voltage drop across the two measurement electrodes (U+ and U-), which is amplified and measured. The electrodes are placed in the visual cortex using a recording chamber filled with saline.

(D) Electronic model of the same situation. The voltage and current electrodes are represented by their respective resistance and capacitance ( $C_u$ ,  $C_c$ ). The impedance of the cortical tissue to the electric flow between the current electrodes is approximated by three general resistances ( $Z_+$ ,  $Z_-$ , and  $Z_T$ ). The resistance  $Z_T$  represents the tissue resistance between the two measurement electrodes (U+ and U-) and is what is measured in the experiments.  $C_s$ , potential stray capacitance between current and voltage electrodes, which could produce crosstalk when not shielded appropriately.

Examining this effect, which is shown in Figure S2, suggested that Pt-Ir electrodes behave not only as a resistor and capacitor in series, but also actually behave like a voltage-stabilizing Zener diode (hence the corresponding electronic symbol in Figure 7D). Only this “active” protection of the electrodes capacitance allows stable current injection and hence an accurate measurement of the impedance.

### The Electric Properties of Cortical Tissue

Our measurements showed that the tissue impedance is frequency independent, allowing the description of cortex as an ohmic resistor. As such, the tissue can be described by its specific electrical resistance (or resistivity). From our data we inferred that the resistance of cortical tissue is in the range of 1.65 to 3.9  $\Omega\text{m}$ , and that of gray matter is between 1.65 and 3.29  $\Omega\text{m}$  (average 2.47  $\Omega\text{m}$ ). These numbers are in good agreement with those obtained in

previous studies. Mitzdorf, for example, found a value of 2.0  $\Omega\text{m}$  for the extracellular space (Mitzdorf, 1985), Ranck reported a range between 2.56 and 3.56  $\Omega\text{m}$  in the rabbit (Ranck, 1963b), and Havstad found values between 3.57 and 4.53  $\Omega\text{m}$  in the cat (Havstad, 1976; Ranck, 1963b). These values suggest that the complex shape and interspersed of cell membranes in the extracellular space set the resistance of cortical tissue to about the four-fold value found in physiological saline, which according to our measurements had a value of 0.664  $\Omega\text{m}$ .

In addition, our measurements show that the resistive properties of the gray matter are largely isotropic, i.e., that the resistivity is the same along each direction. Importantly, we found that the resistance is the same in different directions in the tangential plane, showing that, at a fixed depth, electric propagation is isotropic within a cortical layer. In the radial direction measurements are more difficult, as optimally all four electrodes should be placed

within the gray matter and the voltage electrodes should sample through the different layers. Given the thinness of the gray matter, this is not an easy task. However, our different tests along the radial direction produced numbers comparable to those acquired from measurements in the radial direction. This suggests that the cortical impedance is indeed isotropic. For white matter, in contrast, even two directions within the same plane yielded resistances that differed by a factor of two, demonstrating an anisotropy within this structure. This direction dependency of resistance in white matter might reflect a prominent direction of the fibers, with a lower resistance in the direction of fibers and a higher value orthogonal to this. In fact, the orientation-dependent impedance of the white matter has already been described for the cat brain (Li et al., 1968; Nicholson, 1965).

We mention here in passing that accurate resistivity measurements might offer an approximate assessment of partial volume of extracellular fluid. Assuming that the latter conducts like saline ( $\rho = 0.664 \Omega\text{m}$ ), that neurons are distributed homogeneously, and that the overall conductivity of membrane is very low, the measured gray matter resistivity  $(1.65 \Omega\text{m} + 3.29 \Omega\text{m})/2 = 2.47 \Omega\text{m}$  results in  $0.664 \times 100/2.47 = 27\%$  partial volume for the extracellular fluid in agreement with that described in the literature (Braitenberg and Schuez, 1998; Peters et al., 1991).

The experiments presented in this study were conducted while the visual cortex of the monkeys was in its resting state, i.e., without any concurrent visual stimulation. Earlier studies in cortex (Klvington and Galambos, 1967, 1968) and in hippocampus (Lopez-Aguado et al., 2001) have suggested the possibility of dynamic, sensory, or electrical stimulation-induced resistivity changes that depend on the anatomical architecture and the properties of the local tissue. Resistivity in hippocampus was reported to be layer specific, and so were the impedance changes during activation (Lopez-Aguado et al., 2001). Although in our experiments no systematic attempt was made to measure impedance changes during sensory stimulation, or during electrical stimulation of cortical afferents, we did use a large number of different currents, ranging from 1.25  $\mu\text{A}$  (nonstimulating) to 20  $\mu\text{A}$  (stimulating). No differences in impedance were observed when the tissue was stimulated with these currents (see Figure 1). Future experiments with the five-point technique and whole-spectrum measurements may examine sensory-stimulation-specific effects and layer specificity of resistivity in visual cortex.

### Implications for Modeling and Mapping Neuronal Activity

The frequency independence of tissue impedance clearly shows that the cortex does not act as a frequency filter and does not impose different constraints on the propagation of electric signals of different frequency. Yet, measurements of the spatial correlation of multiunit activity and LFPs routinely reveal stronger and more widespread correlations for slow potentials than for fast oscillations

(Bullock and McClune, 1989; Eckhorn et al., 1988; Steriade and Amzica, 1996). In addition, studies on the stimulus selectivity or tuning properties of different LFP frequency bands often reveal lower selectivity in the low-frequency realm, which appears to be consistent with these being spatially “blurred” compared to the higher frequencies (Frien et al., 2000; Gray et al., 1989; Kayser and Konig, 2004; Liu and Newsome, 2006; Mehring et al., 2003; Rickert et al., 2005; Scherberger et al., 2005; Woelbern et al., 2002).

A reasonable explanation of these results is that the neuronal generators of the signals in different frequency ranges themselves have a distinct size. High-frequency signals, with spiking activity as an extreme example, might arise from very localized clusters of neurons. Lower frequencies could be generated by the mass action of patches, including several columns of neurons, and by the interaction of cortex with subcortical structures (Steriade, 2006). The exploration of the neural structures actually generating neuronal population responses will be of crucial benefit to our understanding of brain function. In fact, it is now well established that single- or multiple-unit activity can be best understood in the context of such population responses, as most of the large variability of stimulus-evoked responses can be attributed to the so-called *ongoing activity* that is most likely induced by neuromodulation and reflects the instantaneous state of cortical networks (Arieli et al., 1996).

Last but not least the methodology presented here may be useful for a direct and precise validation of the conductivity maps generated by noninvasive methods, such as the electrical impedance tomography (EIT), and the electromagnetic source imaging (ESI). Impedance maps are of great interest to both basic and clinical research (e.g., diathermy techniques and dosimetry in the field of electromagnetic biohazards), and there have recently been, once again, efforts to improve the existing techniques or complement them with conductivity measurements relying on surrogate signals, such as those obtained by the well-known variant of magnetic resonance imaging, known as diffusion tensor imaging (DTI, e.g., see Le Bihan et al., 1991). The DTI method relies on the anisotropy of diffusion coefficient in white matter. A similar anisotropy in conductivity exists because of the geometry of neural elements (e.g., orientation of dendrites and axons, formation of dendritic or axonal fascicles, open- and close-field arrangements). Although there is no fundamental relationship between the ionic and water mobilities, the two can have similar conductivity eigenvectors that are imposed by the aforementioned geometrical constraints, and which can be formally linked through the parameterization of the geometric boundary conditions. Diffusion and conductivity anisotropies can indeed be coupled by means of the Nernst-Planck equation that describes the ionic flux through a diffusive membrane, when the flux is under the influence of both ionic and concentration gradients. On the basis of this principle, for instance, it has been shown that a strong linear relationship exists between

the conductivity and diffusion tensor eigenvalues (Tuch et al., 1999, 2001).

## EXPERIMENTAL PROCEDURES

This study involved experiments with two healthy anesthetized monkeys weighing 7.5 and 12 kg, respectively. All studies were carried out with great care to ensure the well-being of the animals, were approved by the local authorities (Regierungspraesidium), and were in full compliance with the guidelines of the European Community (EUVD 86/609/EEC) for the care and use of laboratory animals.

### Implantation of Recording Chamber

The surgical procedures are described in detail elsewhere (Logothetis et al., 2002). Briefly, a skull-form-specific head-holder and recording chamber were made out of MR-compatible PEEK (polyether etherketone; TECAPEEK, Ensinger, Inc., Germany), or medical-grade titanium, and implanted stereotactically on the cranium of each animal under general anesthesia (balanced anesthesia consisting of isoflurane 1.3% and fentanyl 3 g/kg i.v. injections, with 1.8 l/min N<sub>2</sub>O and 1.0 l/min O<sub>2</sub>).

### Recording Protocol

After the animals were premedicated with glycopyrolate (i.m. 0.01 mg/kg) and ketamine (i.m. 15 mg/kg), an intravenous catheter was inserted, and vital monitors (HP OmniCare/CMS; ECG, NIBP, CO<sub>2</sub>, SpO<sub>2</sub>, temperature) were connected. The monkeys were preoxygenated, and anesthesia was induced with fentanyl (3g/kg), thiopental (5 mg/kg), and succinylcholine chloride (3 mg/kg). Following intubation, the animals were ventilated using a Servo Ventilator 900 C (Siemens, Germany), maintaining an end-tidal CO<sub>2</sub> of 33 mmHg and oxygen saturation over 95%. Balanced anesthesia was maintained with end-tidal 0.35% (0.23 MAC for macaques) isoflurane in air and fentanyl (3 g/kg/hr). Muscle relaxation was achieved with mivacurium (5 mg/kg/hr). Body temperature was kept constant, and lactated Ringer's solution was given at a rate of 10 ml/kg/hr. During the entire experiment, the vital signs of the monkey and the depth of anesthesia were continuously monitored.

Two drops of 1% ophthalmic solution of anticholinergic cyclopentolate hydrochloride were instilled into each eye to achieve cycloplegia and mydriasis. Refractive errors were measured, and contact lenses (hard PMMA lenses by Wöhlk GmbH, Germany) with the appropriate dioptric power were used to bring the animal's eye into focus on the stimulus plane.

The position of the stimulation electrodes was determined by recording multiple-unit activity under visual stimulation. The visual stimulator had a resolution of 800 by 600 pixels and a frame rate of 60Hz. Visual search stimuli consisted of drifting gratings, circular checkerboards, and natural stimuli. All measurements were done in the primary visual cortex (area V1) of the monkeys.

### Impedance Measurement Technique

#### General Outline

Figure 7A shows the main components of the impedance measurement setup. Each electrode is encapsulated into an aluminum drive that is attached to a "slide-holder" via a slide. By sliding it up and down, the distance between each guide tube and the skull can be individually adjusted to a minimum. The slide-holder is mounted on the recording chamber with a swivel element. By rotating this holder the horizontal (per convention: approximately mediolateral) and the vertical (approximately anterior-posterior) orientation of the electrode array can be adjusted for measurements along different orientations on the surface of cortex. The electrode is driven by a commercial motor unit (Alpha Omega Engineering, Israel).

The electrode cables are connected to a separately mounted feed-through plate so that plugs can be changed on the plate's backside without the danger of moving the electrode holder and as a result the electrodes in the brain. This allows the investigator to easily connect either the preamplifier unit or the current source and recording system to the electrodes. Preamplifiers and main amplifiers for the recording of neuronal activity during positioning of the electrodes were components of a commercial system (Alpha Omega Engineering, Israel).

#### Current and Measurement Electrodes

Figure 7B displays the layout and electronic devices for the measurement system. Impedance was measured using a four-point technique (also known as Kelvin measurement). The technique was introduced in the bioimpedance field by Schwan in his attempts to deal with electrode polarization (Schwan and Ferris, 1968). It consists of two electrodes for injecting current (outer electrodes I<sub>+</sub> and I<sub>−</sub>) and two electrodes for measuring voltage (inner electrodes U<sub>+</sub> and U<sub>−</sub>). An excitation current generated by a current source flows through the outer electrodes I<sub>+</sub>, I<sub>−</sub>, resulting in three-dimensional current flow in the tissue. This leads to a potential difference between the voltage electrodes that is proportional to the tissue impedance (Figure 7D). This scheme can be approximated by three general impedances (Z<sub>+</sub>, Z<sub>T</sub>, and Z<sub>−</sub>; Figure 7D). The tissue impedance can be measured—unaffected by the electrodes' own impedance—by recording the voltage drop across Z<sub>T</sub>, provided that input impedances as well as the differential and common-mode rejection of the voltage amplifier are infinite. We therefore built a measurement amplifier with very high impedance input (10 GΩ) to avoid reduction of the voltage signal at low frequencies and to preclude any current that could charge the electrode capacitors C<sub>U+</sub> and C<sub>U−</sub> (see below).

The high impedance of the metal microelectrodes underlying their frequency-dependent conductivity is represented by the capacitors at their tips (Figure 7D) and is mainly due to the very small metal-electrolyte interface at the electrode tip (Geddes, 1997). In addition, the current-injecting electrodes are represented by their impedances as well as a parallel Zener diode, which reflects the rectifying properties of metal microelectrodes under current load (Robinson, 1968). We used glass-coated platinum-iridium electrodes (Thomas Recording, GmbH, Giessen), which were additionally stiffened 3 mm behind the tip with polyamide-coated glass tubes. These tubes ran inside the guide tube of the drive. The guide tube was attached via an isolating thread in the drive to avoid ground loops (see crosstalk section). This arrangement ensured complete shielding of all parts connected to the electrodes.

#### Grounding and Interference Minimization

This four-electrode configuration eliminates the effects of an electrode's own impedance on tissue impedance. The technique is very accurate if electrode impedances are low (on the order of a few hundred ohms). To achieve accurate placement of the electrodes at the desired position in cortex, we monitored multiple-unit activity at the electrodes before making impedance measurements. This required electrode impedances that are approximately 3 orders of magnitude greater, namely a few hundred kΩ. Such high-impedance electrodes, however, have an even higher impedance at lower frequencies due to the frequency dependence of the electrode capacitance (Geddes, 1997; Robinson, 1968; Schwan, 1963; Schwan and Ferris, 1968); for example, an electrode with an impedance of 100 kΩ at 1 kHz has an impedance of 10 MΩ at 10 Hz (assuming a 1/ωC relation). Such high impedance renders the electrodes very sensitive to interference (e.g., 50 Hz). In addition, the four-electrode configuration lacks a low-resistive connection between the animal and the circuit ground. Such a connection is needed so that all interferences that the animal picks up from the surrounding can flow via the low-resistance connection to ground, instead of flowing via the electrodes. Configuring the system so that one of the current electrodes is the circuit ground does not solve the problem, as a potential dynamic asymmetrical load at the current electrodes could load the other current electrode



with the relatively high stray capacitance of the animal, and therefore lower the effective current through the tissue.

To address all these concerns, we used a custom-made “current isolation unit” consisting of two voltage-to-current converters with  $+10 \mu\text{A/V}$  and  $-10 \mu\text{A/V}$  output currents (Figure 7B) and a fifth conductor as the general instrument ground (Gnd, Figure 7C). This simulates a floating current source, as typically used for electrical microstimulation, by having two separate sources with opposite sign, where each is referenced to ground. The voltage-to-current converters were driven by the output of the dynamic signal analyzer (HP, 35670A) via a voltage buffer. The fifth conductor (circuit ground) was connected to the low-resistive metallic head post (Figure 7B) or inserted into the tissue by means of a subcutaneous needle. In this configuration, the animal serves as a shield (buffer) against interference, and an active stray capacitance compensation circuit for every electrode and its connection line can be used to avoid capacitive shunting of the electrode signals to ground.

#### Reduction of Crosstalk

A number of factors, including the configuration of electrodes and the wires connecting them to the amplifiers, make the impedance measurements highly susceptible to crosstalk. Such crosstalk would result from the capacitive coupling of current and voltage electrodes, represented by  $C_s$  in Figure 7C, and hence superimpose additional signals (proportional to the voltages on the current electrodes) onto the voltage signal picked up from the tissue. Specifically, (1) the distance between the electrodes and their connecting wires is very small (1 mm), (2) the impedance of the voltage electrodes is high (on the order of 100 k $\Omega$ ), (3) the measured voltages are very low (1 mV), and (4) the voltage on the current electrodes is relatively high (2V).

To eliminate the effect of  $C_s$  (crosstalk) all wires were shielded and the shields were connected to the circuit ground. In addition, the guide tubes with the electrodes were grounded indirectly by immersion in the saline filling of the recording chamber. The saline is conductive and connects the guide tubes with the animal and via its ground contact to circuit ground. This loop was made to prevent the guide tubes from short-circuiting the brain regions around the current electrodes near the dura. When the guide tubes are connected directly to circuit ground, a fraction of the injected currents can flow from the electrode tip to its nearby guide tube, from there to the circuit ground, to the guide tube of the opposite current-electrode guide tube, and then finally to the electrode tip. This “detour current” may be frequency dependent and erroneously diminish a potential flat frequency response. In the region of the electrode that is in saline or is embedded in the tissue, the saline and the tissues themselves serve as a shield that prevents crosstalk.

#### Cable Capacitance Minimization

Additional sources of measurement error are the capacitances between the electrodes and their shielding. A capacitance from a current electrode to ground would lower the excitation current, especially for high frequencies and high impedance current electrodes. This will lead to a frequency-dependent decrease in the resistance reading. A capacitance from a voltage electrode to ground would decrease the input voltage of the amplifier, lowering the resistance reading, although in a first approximation this effect is not frequency dependent. To circumvent these potential sources of error, all four electrode lines were endowed with their own active cable-capacitance compensation circuit (CC, Figure 7B, inset) that reduces the capacitance to approximately 10 pF.

#### Measurement and Analysis

The injected current was proportional to a control voltage delivered by a signal generator. The voltage-to-current converter produced a current,  $I$ , whose relationship to the applied control voltage is given by the equation  $I = U_{\text{drive}}/100 \text{ k}\Omega$ . The voltage difference during the application of the excitation current was measured between the two voltage electrodes ( $U_+$ ,  $U_-$ ). The signals from these electrodes were high-pass filtered to remove DC fluctuations and amplified by a factor of 100 with a conventional instrumentation amplifier (Figure 7B). The cut-off fre-

quency of the filter was low (0.0016 Hz) to avoid phase shifts at low frequencies (e.g., 1 Hz).

For analysis, the signal driving the current converters (target signal) was fed to the first ( $U_{\text{drive}}$ ), and the filtered and amplified signal of the voltage (recording) electrodes to the second ( $U_{\text{rec}}$ ) input of a signal analyzer (HP 35670A, Agilent Technologies Inc., USA). The analyzer computed both the  $U_{\text{rec}}/U_{\text{drive}}$  ratio and the phase shift between the two signals. The  $U_{\text{rec}}/U_{\text{drive}}$  quotient is proportional to the resistance  $Z_T = U_T/I$ , as can be seen by taking into account an amplification factor of 100 ( $U_{\text{rec}} = 100 * U_T$ ) and the relation between driving voltage and the applied current (see above):

$$U_{\text{rec}}/U_{\text{drive}} = (100 * U_T)/(I * 100 \text{ k}\Omega) = Z_T/1000 \Omega.$$

In all figures, the effects of frequency on the tissue resistivity are expressed as  $\text{dB} = 20 \log(U_{\text{rec}}/U_{\text{drive}}) = 20 \log(Z_T/1000 \Omega)$  and/or in Ohm (the value of  $Z_T$ ).

#### System Performance

The proper functioning of metal microelectrodes can be negatively affected by electrochemical processes occurring at the electrode tip, which can change the electrode impedance in complex ways (Geddes, 1997; Helmholtz, 1879; Warburg, 1899). To ensure valid measurements after each repositioning of the electrodes, the voltage-to-current converter was connected to a waveform generator, and a rectangular waveform with 100 Hz was used to drive the current source, with a current of 20  $\mu\text{A}$  peak value (Figure S2). The upper panel of Figure S2 shows the voltage of the  $I_+$  electrode referenced to ground during the application of this current. The slope of the voltage signal is due to the capacitive behavior of the metal microelectrodes (Robinson, 1968). After charging this capacitor a clipping behavior is observed like that known for Zener diodes. This clipping behavior manifests as a slow increase of the applied voltage (in contrast to the initial sharp transient rise). If there was no such clipping, the voltage would quickly rise to the limits of the stimulation system. Importantly, this clipping of the current electrodes is essential for measuring down to lower frequencies, as can be seen from Figure S2. If the cycle time of the stimulating current becomes too long, the slow rise of the voltage continues long enough to reach the limits of the system, hence compromising proper stimulation. Our present setup allowed measurements down to frequencies of 10 Hz; for lower frequencies, electrodes with lower impedance would have to be used. Yet, such electrodes would no longer allow the simultaneous assessment of neuronal activity, which was required for the accurate placement of the electrodes (see text above). The clipping behavior was clearly evident with platinum and copper electrodes, but with tungsten electrodes it was poor and stable only below a certain current and only for a certain time; in fact, with tungsten electrode the stimulation voltage reached the system's limits within few ms. The maximum current for which clipping occurs is higher for lower impedance electrodes, and it is higher in saline than in the brain. It is necessary to supervise the voltage across the current electrodes during the experiment and stop the measurements when the clipping disappears and the current source saturates.

The middle panel of Figure S2 shows the voltage at the ( $I_-$ ) electrode, which has the opposite sign, as expected. The clear dissimilarity of the waveform at the voltage and current electrodes is additional evidence for successful compensation of the crosstalk. The waveform of the voltage at the current electrodes was found to depend on the particular electrode, its impedance, and the signal frequency; this waveform may change during the experiment. As far as the precision of the spectrum measurement was concerned, however, such changes were insignificant for voltages within the output voltage range of the current source ( $\pm 9\text{V}$ ). The lower panel in that figure shows the voltage actually measured across the voltage electrodes ( $U_+$  and  $U_-$ ); it has the same rectangular shape as the applied current, as expected from a flat frequency response.

# Supplemental Data

The Supplemental Data for this article can be found online at <http://www.neuron.org/cgi/content/full/55/5/809/DC1/>.

# ACKNOWLEDGMENTS

The authors thank Mark Augath and Diane Blaurock for many helpful comments on the manuscript and Dr. Jon Pauls for assisting in the experiments. Special thanks to Dr. Christof Koch for his helpful comments and suggestions on the final draft of the manuscript. The study was supported by the Max Planck Society.

Received: June 5, 2007

Revised: July 13, 2007

Accepted: July 24, 2007

Published: September 5, 2007

# REFERENCES

- Abeles, M. (1991). *Corticonics. Neural Circuits of the Cerebral Cortex* (Cambridge: Cambridge University Press).
- Adrian, E.D., and Zotterman, Y. (1926). The impulses produced by sensory nerve-endings, part 2. The response of a single end-organ. *J. Physiol.* **61**, 151–171.
- Aidley, D.J. (1989). *The Physiology of Excitable Cells* (Cambridge: Cambridge University Press).
- Ajmone-Marsan, C. (1965). Electrical activity of the brain: Slow waves and neuronal activity. *Isr. J. Med. Sci.* **1**, 104–117.
- Arieli, A., Sterkin, A., Grinvald, A., and Aertsen, A. (1996). Dynamics of ongoing activity: Explanation of the large variability in evoked cortical responses. *Science* **273**, 1868–1871.
- Bedard, C., Kroger, H., and Destexhe, A. (2004). Modeling extracellular field potentials and the frequency-filtering properties of extracellular space. *Biophys. J.* **86**, 1829–1842.
- Bedard, C., Kroger, H., and Destexhe, A. (2006). Model of low-pass filtering of local field potentials in brain tissue. *Phys. Rev. E Stat. Nonlin. Soft Matter Phys.* **73**, 051911.
- Braitenberg, V., and Schuez, A. (1998). *Cortex: Statistics and Geometry of Neuronal Connectivity* (Berlin: Springer).
- Buchwald, J.S., Hala, E.S., and Schramm, S. (1965). A comparison of multi-unit activity and EEG activity recorded from the same brain site in chronic cats during behavioral conditioning. *Nature* **205**, 1012–1014.
- Bullock, T.H. (1997). Signals and signs in the nervous system: The dynamic anatomy of electrical activity is probably information-rich. *Proc. Natl. Acad. Sci. USA* **94**, 1–6.
- Bullock, T.H., and McClune, M.C. (1989). Lateral coherence of the electrocorticogram: A new measure of brain synchrony. *Electroencephalogr. Clin. Neurophysiol.* **73**, 479–498.
- Buzsaki, G. (2002). Theta oscillations in the hippocampus. *Neuron* **33**, 325–340.
- Chrobak, J.J., Lorincz, A., and Buzsaki, G. (2000). Physiological patterns in the hippocampo-entorhinal cortex system. *Hippocampus* **10**, 457–465.
- Creutzfeldt, O.D., Watanabe, S., and Lux, H.D. (1966). Relations between EEG phenomena and potentials of single cortical cells. I. Evoked responses after thalamic and epicortical stimulation. *Electroencephalogr. Clin. Neurophysiol.* **20**, 1–18.
- Destexhe, A. (1998). Spike-and-wave oscillations based on the properties of GABAB receptors. *J. Neurosci.* **18**, 9099–9111.
- Destexhe, A., Contreras, D., and Steriade, M. (1999). Spatiotemporal analysis of local field potentials and unit discharges in cat cerebral cortex during natural wake and sleep states. *J. Neurosci.* **19**, 4595–4608.

- Douglas, R.J., Martin, K.A.C., and Whitteridge, D. (1989). A functional microcircuit for cat visual cortex. *Neural Comput.* **1**, 480–488.
- Douglas, R.J., and Martin, K.A.C. (1990). Neocortex. In *The Synaptic Organization of the Brain*, G.M. Shepherd, ed. (Oxford: Oxford University Press), pp. 389–438.
- Douglas, R.J., and Martin, K.A. (1991). A functional microcircuit for cat visual cortex. *J. Physiol.* **440**, 735–769.
- Eccles, J.C. (1951). Interpretation of action potentials evoked in the cerebral cortex. *Electroencephalogr. Clin. Neurophysiol.* **3**, 449–464.
- Eckhorn, R., Bauer, R., Jordan, W., Brosch, M., Kruse, W., Munk, M., and Reitboeck, H.J. (1988). Coherent oscillations: A mechanism of feature linking in the visual cortex? Multiple electrode and correlation analyses in the cat. *Biol. Cybern.* **60**, 121–130.
- Freeman, W.J. (1975). *Mass Action in the Nervous System* (New York: Academic Press).
- Freygang, W.H., and Landau, W.M. (1955). Some relations between resistivity and electrical activity in the cerebral cortex of the cat. *J. Cell. Comp. Physiol.* **45**, 377–392.
- Frien, A., Eckhorn, R., Bauer, R., Woelbern, T., and Gabriel, A. (2000). Fast oscillations display sharper orientation tuning than slower components of the same recordings in striate cortex of the awake monkey. *Eur. J. Neurosci.* **12**, 1453–1465.
- Fromm, G.H., and Bond, H.W. (1967). The relationship between neuron activity and cortical steady potentials. *Electroencephalogr. Clin. Neurophysiol.* **22**, 159–166.
- Geddes, L.A. (1997). Historical evolution of circuit models for the electrode-electrolyte interface. *Ann. Biomed. Eng.* **25**, 1–14.
- Geddes, L.A., Da Costa, C.P., and Wise, G. (1971). The impedance of stainless-steel electrodes. *Medical & Biological Engineering* **9**, 511–521.
- Gold, C., Henze, D.A., Koch, C., and Buzsaki, G. (2006). On the origin of the extracellular action potential waveform: A modeling study. *J. Neurophysiol.* **95**, 3113–3128.
- Gray, C.M., Konig, P., Engel, A.K., and Singer, W. (1989). Oscillatory responses in cat visual cortex exhibit inter-columnar synchronization which reflects global stimulus properties. *Nature* **338**, 334–337.
- Havstad, J.W. (1976). *Electrical impedance of cerebral cortex: An experimental and theoretical investigation*. PhD thesis, Stanford University, Stanford, California.
- Helmholtz, H. (1879). Studien ueber electrische Grenzschichten. *Ann. Phys. Chem.* **7**, 337–382.
- Hubel, D.H., and Wiesel, T.N. (1962). Receptive fields, binocular interaction and functional architecture in the cat's visual cortex. *J. Physiol.* **160**, 106–154.
- Johnston, D., and Wu, S.M. (1995). *Foundations of Cellular Neurophysiology* (Cambridge, MA: MIT Press).
- Kayser, C., and Konig, P. (2004). Stimulus locking and feature selectivity prevail in complementary frequency ranges of V1 local field potentials. *Eur. J. Neurosci.* **19**, 485–489.
- Klvington, K.A., and Galambos, R. (1967). Resistance shifts accompanying evoked cortical response in cat. *Science* **157**, 211.
- Klvington, K.A., and Galambos, R. (1968). Rapid resistance shifts in cat cortex during click-evoked responses. *J. Neurophysiol.* **31**, 565–573.
- Koch, C., and Segev, I. (1998). *Methods in Neuronal Modeling* (Cambridge, MA: MIT Press).
- Kuffler, S.W. (1953). Discharge patterns and functional organization of the mammalian retina. *J. Neurophysiol.* **16**, 37–68.
- Le Bihan, D., Turner, R., Moonen, C.T., and Pekar, J. (1991). Imaging of diffusion and microcirculation with gradient sensitization: Design, strategy, and significance. *J. Magn. Reson. Imaging* **1**, 7–28.

- Lettvin, J.Y., Maturana, H.R., McCulloch, W.S., and Pitts, W.H. (1959). What the frog's eye tells the frog's brain. *Proc. Inst. Radio. Engrs.* 47, 1940–1951.
- Li, C.L., Bak, A.F., and Parker, L.O. (1968). Specific resistivity of cerebral cortex and white matter. *Exp. Neurol.* 20, 544–557.
- Liu, J., and Newsome, W.T. (2006). Local field potential in cortical area MT: Stimulus tuning and behavioral correlations. *J. Neurosci.* 26, 7779–7790.
- Logothetis, N.K. (2002). The neural basis of the blood-oxygen-level-dependent functional magnetic resonance imaging signal. *Philos. Trans. R. Soc. Lond. B Biol. Sci.* 357, 1003–1037.
- Logothetis, N.K., Pauls, J., Augath, M., Trinath, T., and Oeltermann, A. (2001). Neurophysiological investigation of the basis of the fMRI signal. *Nature* 412, 150–157.
- Logothetis, N.K., Merkle, H., Augath, M., Trinath, T., and Ugurbil, K. (2002). Ultra high-resolution fMRI in monkeys with implanted RF coils. *Neuron* 35, 227–242.
- Logothetis, N.K., and Wandell, B.A. (2004). Interpreting the BOLD signal. *Annu. Rev. Physiol.* 66, 735–769.
- Lopez-Aguado, L., Ibarz, J.M., and Herreras, O. (2001). Activity-dependent changes of tissue resistivity in the CA1 region in vivo are layer-specific: Modulation of evoked potentials. *Neuroscience* 108, 249–262.
- Lorente de Nó, R. (1947). A study of nerve physiology, Part 2, Chapter XVI. Analysis of the distribution of action currents of nerve in volume conductors. *Studies from the Rockefeller Institute Medical Res.* 132, 384–477.
- McIntyre, C.C., and Grill, W.M. (2001). Finite element analysis of the current-density and electric field generated by metal microelectrodes. *Ann. Biomed. Eng.* 29, 227–235.
- Mehring, C., Rickert, J., Vaadia, E., Cardoso de Oliveira, S., Aertsen, A., and Rotter, S. (2003). Inference of hand movements from local field potentials in monkey motor cortex. *Nat. Neurosci.* 6, 1253–1254.
- Mitzdorf, U. (1985). Current source-density method and application in cat cerebral cortex: Investigation of evoked potentials and EEG phenomena. *Physiol. Rev.* 65, 37–100.
- Morocutti, C., Sommer-Smith, J.A., and Creutzfeldt, O. (1966). The visual reaction potential in normal experimental people and characteristic changes in epileptics. *Arch. Psychiatr. Nervenkr.* 208, 234–254.
- Nadasdy, Z., Csicsvari, J., Penttonen, M., Hetke, J., Wise, K., and Buzsáki, G. (1998). Extracellular recording and analysis of neuronal activity: From single cells to ensembles. In *Neuronal Ensembles: Strategies from Recording and Decoding*, H. Eichenbaum and J.L. Davis, eds. (New York: Wiley-Liss), pp. 17–55.
- Nicholson, P.W. (1965). Specific impedance of cerebral white matter. *Exp. Neurol.* 13, 386–401.
- Niessing, J., Ebisch, B., Schmidt, K.E., Niessing, M., Singer, W., and Galuske, R.A.W. (2005). Hemodynamic signals correlate tightly with synchronized gamma oscillations. *Science* 309, 948–951.
- Nunez, P.L. (1981). *Electric Fields in the Brain. The Neurophysics of EEG* (Oxford: Oxford University Press).
- Nunez, P.L. (1994). *Neocortical Dynamics and Human EEG Rhythms* (Oxford: Oxford University Press).
- Peters, A., Palay, S.L., and Webster, H.F. (1991). *The Fine Structure of the Nervous System* (Oxford: Oxford University Press).
- Rall, W., and Shepherd, G.M. (1968). Theoretical reconstruction of field potentials and dendrodendritic synaptic interactions in olfactory bulb. *J. Neurophysiol.* 31, 884–915.
- Ranck, J.B. (1963a). Analysis of specific impedance of rabbit cerebral cortex. *Exp. Neurol.* 7, 153–174.
- Ranck, J.B. (1963b). Specific impedance of rabbit cerebral cortex. *Exp. Neurol.* 7, 144–152.
- Rickert, J., Oliveira, S.C., Vaadia, E., Aertsen, A., Rotter, S., and Mehring, C. (2005). Encoding of movement direction in different frequency ranges of motor cortical local field potentials. *J. Neurosci.* 25, 8815–8824.
- Robinson, D.A. (1968). The electric properties of metal microelectrodes. *Proc. IEEE* 56, 1065–1071.
- Scherberger, H., Jarvis, M.R., and Andersen, R.A. (2005). Cortical local field potential encodes movement intentions in the posterior parietal cortex. *Neuron* 46, 347–354.
- Schwan, H.P. (1963). Determination of Biological Impedances. In *Physical Techniques in Biological Research*, W.L. Nastuk, ed. (New York: Academic Press), pp. 323–407.
- Schwan, H.P. (1966). Alternating current electrode polarization. *Biophysik* 3, 181–201.
- Schwan, H.P. (1968). Electrode polarization impedance and measurements in biological materials. *Ann. N Y Acad. Sci.* 148, 191–209.
- Schwan, H.P. (1999). The practical success of impedance techniques from an historical perspective. *Electrical bioimpedance methods. Applications to Medicine and Biotechnology* 873, 1–12.
- Schwan, H.P., and Ferris, C.D. (1968). 4-Electrode null techniques for impedance measurement with high resolution. *Rev. Sci. Instrum.* 39, 481.
- Steriade, M. (2006). Grouping of brain rhythms in corticothalamic systems. *Neuroscience* 137, 1087–1106.
- Steriade, M., and Amzica, F. (1996). Intracortical and corticothalamic coherency of fast spontaneous oscillations. *Proc. Natl. Acad. Sci. USA* 93, 2533–2538.
- Tuch, D.S., Wedeen, V.J., Dale, A.M., George, J.S., and Belliveau, J.W. (1999). Conductivity mapping of biological tissue using diffusion MRI. *Ann. N Y Acad. Sci.* 888, 314–316.
- Tuch, D.S., Wedeen, V.J., Dale, A.M., George, J.S., and Belliveau, J.W. (2001). Conductivity tensor mapping of the human brain using diffusion tensor MRI. *Proc. Natl. Acad. Sci. USA* 98, 11697–11701.
- Van Harrevel, A., and Ochs, S. (1956). Cerebral impedance changes after circulatory arrest. *Am. J. Physiol.* 187, 180–192.
- Van Harrevel, A., Murphy, T., and Nobel, K.W. (1963). Specific impedance of rabbit's cortical tissue. *Am. J. Physiol.* 205, 203–207.
- Warburg, E. (1899). Über das Verhalten sogenannter unpolarisierbarer Elektroden gegen Wechselstrom. *Ann. Phys. Chem.* 67, 493–499.
- Watanabe, S., Konishi, M., and Creutzfeldt, O.D. (1966). Postsynaptic potentials in the cat's visual cortex following electrical stimulation of afferent pathways. *Exp. Brain Res.* 1, 272–283.
- Wilke, M., Logothetis, N.K., and Leopold, D.A. (2006). Local field potential reflects perceptual suppression in monkey visual cortex. *Proc. Natl. Acad. Sci. USA* 103, 17507–17512.
- Woelbern, T., Eckhorn, R., Frien, A., and Bauer, R. (2002). Perceptual grouping correlates with short synchronization in monkey prestriate cortex. *Neuroreport* 13, 1881–1886.